Compensation of spectral and RF errors in swept-source OCT for high extinction complex demodulation

Meena Siddiqui,[1,2,3] Serhat Tozburun,[2,3] Ellen Ziyi Zhang,[2,3] and Benjamin J. Vakoc[1,2,3]

[1] *Harvard-MIT Division of Health Sciences and Technology, Cambridge, Massachusetts 02139, USA*
[2] *Wellman Center for Photomedicine, MGH, Boston, Massachusetts 02114, USA*
[3] *Harvard Medical School, Boston, Massachusetts 02115, USA*
**siddiqui@mit.edu*

Abstract: We provide a framework for compensating errors within passive optical quadrature demodulation circuits used in swept-source optical coherence tomography (OCT). Quadrature demodulation allows for detection of both the real and imaginary components of an interference fringe, and this information separates signals from positive and negative depth spaces. To achieve a high extinction ($\sim$60 dB) between these positive and negative signals, the demodulation error must be less than 0.1% in amplitude and phase. It is difficult to construct a system that achieves this low error across the wide spectral and RF bandwidths of high-speed swept-source systems. In a prior work, post-processing methods for removing residual spectral errors were described. Here, we identify the importance of a second class of errors originating in the RF domain, and present a comprehensive framework for compensating both spectral and RF errors. Using this framework, extinctions $>$60 dB are demonstrated. A stability analysis shows that calibration parameters associated with RF errors are accurate for many days, while those associated with spectral errors must be updated prior to each imaging session. Empirical procedures to derive both RF and spectral calibration parameters simultaneously and to update spectral calibration parameters are presented. These algorithms provide the basis for using passive optical quadrature demodulation circuits with high speed and wide-bandwidth swept-source OCT systems.

OCIS codes: (110.4500) Optical Coherence Tomography; (120.3180) Interferometry; (100.0100) Image Processing.

References and links

1. M. Wojtkowski, A. Kowalczyk, R. Leitgeb, and A.F. Fercher, "Full range complex spectral optical coherence tomography technique in eye imaging," Opt. Lett. **27,** 1415–1417 (2002).
2. Y. Zhao, Z. Chen, Z. Ding, H. Ren, and J.S. Nelson, "Real-time phase-resolved functional optical coherence tomography by use of optical Hilbert transform," Opt. Lett. **27,** 98–100 (2002).
3. R.A. Leitgeb, C.K. Hitzenberger, A.F. Fercher, and T. Bajraszewski, "Phase-shifting algorithm to achieve high-speed long-depth-range probing by frequency-domain optical coherence tomography," Opt. Lett. **28,** 2201–2203 (2003).
4. P. Targowski, M. Wojkowski, A. Kowalczyk, T. Bajraszewski, M. Szkulmowski, and I. Gorczyska, "Complex spectral OCT in human eye imaging in vivo," Opt. Commun. **229,** 79–84 (2004).

#230495 - $15.00 USD Received 12 Dec 2014; revised 16 Jan 2015; accepted 17 Jan 2015; published 23 Feb 2015

5. E. Gotzinger, M. Pircher, R.A. Leitgeb, and C.K. Hitzenberger, "High speed full range complex spectral domain optical coherence tomography," Opt. Express **13,** 583–594 (2005).
6. S.H. Yun, G.J. Tearner, J.F. de Boer, and B.E Bouma, "Removing the depth-degeneracy in optical frequency domain imaging with frequency shifting," Opt. Express **12,** 4822–4828 (2004).
7. M. Sarunic, M.A. Choma, C. Yang, and J.A. Izatt, "Instantaneous complex conjugate resolved spectral domain and swept-source OCT using 3x3 fiber couplers," Opt. Express **13,** 957–967 (2005).
8. B.J. Vakoc, S.H. Yun, G.J. Tearney, and B.E. Bouma, "Elimination of depth degeneracy in optical frequency-domain imaging through polarization-based optical demodulation," Opt. Lett. **31,** 362–364 (2006).
9. N. Lippok, S. Coen, R. Leonhardt, P. Nielsen, and F. Banholsbeeck, "Instantaneous quadrature components or Jones vector retrieval using the Pancharatnam-Berry phase in frequency domain low-coherence interferometry," Opt. Lett. **37,** 3102–3104 (2012).
10. S. Tozburun, M. Siddiqui, and B.J. Vakoc, "A rapid, dispersion-based wavelength-stepped and wavelength-swept laser for optical coherence tomography," Opt. Express **22,** 3414–3424 (2014).
11. B.J. Vakoc, S.H. Yun, J.F. de Boer, G.J. Tearney, and B.E. Bouma, "Phase-resolved optical frequency domain imaging," Opt. Express **13,** 5483–5493 (2005).
12. S.H. Yun, G.J. Tearney, J.F. de Boer, N Iftimia, and B.E. Bouma, "High-speed optical frequency-domain imaging," Opt. Express **11,** 2953–2963 (2003).

1. Introduction

Without complex demodulation, Fourier domain optical coherence tomography (FD-OCT) cannot differentiate between signals located at an equivalent distance above and below the zero-delay location. This leads to a depth ambiguity (alternatively termed complex conjugate ambiguity or depth degeneracy). If the sample is physically located entirely on one side of the zero delay position, this ambiguity does not induce imaging artifacts. However, for many applications, it is preferable to use both the positive and negative depth space to achieve a larger imaging range. In these applications, complex demodulation is used to discriminate between positive and negative depth space signals.

There are many implementations of complex demodulation in OCT. Phase-shifting methods were the first attempt to achieve full-range OCT. However these methods did not provide high extinction, and required multiple A-lines per measurement location [1–4]. Later, simultaneous detection of real and imaginary fringe components were achieved by interferometer modifications. A common technique is to use an active phase modulating element in the sample or reference arm. These include configurations based on phase modulators [5] and acousto-optic frequency shifters (AOFS) [6]. While the AOFS method is straightforward to implement, it has several limitations. First, AOFS devices operate over a finite optical bandwidth, limiting their utility in wide-band OCT systems. Second, the AOFS drive frequency is optimal at 1/4 the digitizer acquisition clock. This necessitates a change in AOFS hardware if the acquisition clock is changed. Finally, the AOFS method doubles the required digitizer bandwidth per channel. For some applications, this doubling of the digitizer bandwidth while keeping the same number of channels is advantageous. While in others (i.e. high speed systems operating near the digitizer maximum speed) it may be advantageous to keep the same RF bandwidth and add a quadrature signal on a second digitizer channel. Passive optical demodulation approaches exist for acquiring this quadrature information [7–9].

Generating accurate quadrature signals has been a challenge for passive optical quadrature demodulation circuits. With imperfect quadrature demodulation, a mirror will generate signal power on both sides of the zero delay position. To match the 60 dB extinction provided by AOFS and required in many applications, quadrature errors below one part per thousand (0.1%) are required (errors scale with the $\sqrt{\text{extinction}}$). In a previous work, we demonstrated a polarization-based demodulation circuit that created quadrature relationships by manipulating the light polarization within an optical circuit [8]. Because the birefringent properties of the demodulation circuit vary as a function of wavenumber, a quadrature correction algorithm was implemented in post-processing to reduce the signal power on one side of zero delay, and in-

#230495 - $15.00 USD Received 12 Dec 2014; revised 16 Jan 2015; accepted 17 Jan 2015; published 23 Feb 2015

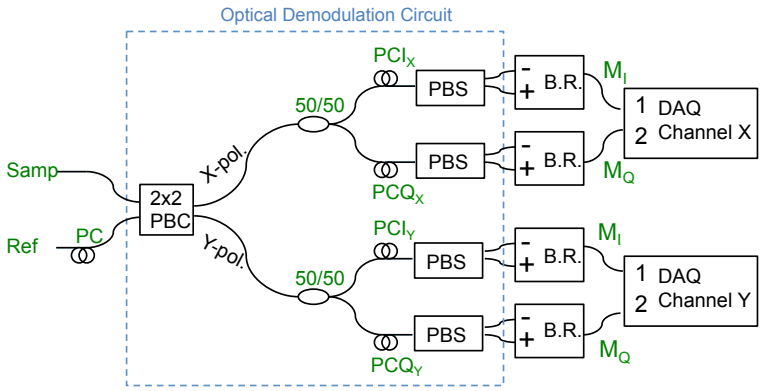

Fig. 1. Schematic of a polarization-based quadrature demodulation circuit with polarization diversity and balanced detection. Components contained within the blue dotted box are part of the optical demodulation circuit. PC$_I$ = in-phase polarization controller, PC$_Q$ = quadrature polarization controller, M_I = measured in-phase signal, M_Q = measured quadrature signal, PBS/PBC = polarization beam splitter/combiner.

crease the power on the other. As a result, an extinction ratio greater than 50 dB was achieved for a low-speed (10 kHz A-line rate) swept-source system.

Here, we expand on this earlier work by identifying a second source of error that is dependent on the fringe RF frequency rather than wavenumber. The magnitude of this noise scales with the RF bandwidth, and will be limiting for high-speed imaging systems operating in the 100 to 1000 MHz RF signal range (the prior system operated with 10 MHz bandwidth, and the effect of this RF error was small). These RF domain errors cannot be corrected with existing algorithms. In this work, we describe the origin of these RF errors and present a combined quadrature correction framework that addresses both wavenumber-dependent (spectral) and RF-dependent errors. We demonstrate that RF errors are created by path length mismatches in the demodulation circuit and non-flat electronic RF filtering, and that these errors are stable in time (and may only need to be derived once for a given system). By contrast, spectral errors vary with system temperature and remain valid for several to tens of minutes. Therefore, two methods to derive correction parameters empirically from mirror signals are presented. The performance of these methods including their stability are presented for a polarization-based demodulation circuit. However, these methods are generalizable to other passive quadrature demodulation schemes used in swept-source OCT.

2. Experimental system design

2.1. Polarization-based demodulation circuit

The polarization-based demodulation circuit is presented in Fig. 1 [8]. This quadrature demodulation is independent of changes in the light amplitude, phase, or polarization that occur within the reference or sample arm. The device is constructed entirely with fiber-based components including a 50/50 fused coupler (Gould Fiber Optics), five polarization beam splitters/combiners (PBS/PBC) (Oz Optics 1x2 and 2x2), and polarization controllers (PCs)(General Photonics). No polarization-maintaining fibers were used within the circuit or interferometer. In addition to providing quadrature signals, this circuit supports both balanced-detection (to reduce laser amplitude noise and autocorrelation noise) and polarization diverse detection. As in other polarization diverse circuits, the sample arm light is returned in both the X and Y polarization

#230495 - $15.00 USD Received 12 Dec 2014; revised 16 Jan 2015; accepted 17 Jan 2015; published 23 Feb 2015

states and is directed to separate detector subcircuits for independent detection. Here, sample arm light returning in the X polarization is directed to the channel X subcircuit (after the 2x2 PBC), and sample light in the orthogonal Y polarization is directed to the channel Y subcircuit. Note that the sample arm light and the reference arm light are orthogonally polarized in each of the 2x2 PBC output fibers thus there is no interference at this 2x2 PBC. Once these optical signals pass through the second PBS, interference signals are generated and the amplitude and phase of these signals are determined by the specific orientation of the polarizations relative to the PBS axis. By controlling the birefringence of the fiber between the 2x2 PBC and 1x2 PBSs with the PCs, it is possible to tune the interference amplitude and phase relationship of one interference fringe (M_I) relative to the other (M_Q).

Amplitude noise is removed by balanced detection of complementary outputs from each 1x2 PBS. We note that the demodulation properties of the circuit are based on the optical properties within the circuit, and are independent of the interferometer sample arm. Thus, the demodulation of Channel X is independent of changes to the sample arm light (or the reference arm light). This decouples the demodulation from the varying properties of the interferometer and sample. The fibers connecting the 1x2 PBSs and the detectors only transmit power and are not phase or birefringence sensitive.

Nominally, all the PCs are configured such that the reference arm power is equally distributed to each output of the 1x2 PBS, and the interference signals are approximately equal in amplitude and phase shifted by 90 degrees. To achieve this, the following procedure was used. First, reference arm power was equally split between the X and Y subcircuits using the PC within the reference arm (before the 2x2 PBC). Next, a sample arm mirror signal was provided to generate a single depth fringe. The PCI_X of the X subcircuit was then configured to achieve equal reference arm power at the output of its 1x2 PBS, which will also maximized the interference fringe amplitude. Then, the PCQ_X of the X subcircuit was configured to provide equal reference arm power on each of its 1x2 PBS outputs (which again maximized fringe amplitude). The controllers PCI_X and PCQ_X were perturbed to induce an approximate 90 degree phase shift relative to each other while maintaining high fringe amplitude. Once obtained, this sets the physical state of the X subcircuit. The same procedure can be applied independently to the Y subcircuit. It is not essential that the phase shift be accurately set to 90 degrees as these errors will be removed in post-processing. Therefore, care is taken to ensure that fringe amplitudes remain high and reference arm powers balanced while setting the phase relationship approximately to 90 degrees.

2.2. OCT system

To validate this method, we used two imaging systems. The first used a polygon-based swept-source operating at 46.8 kHz and two balanced receivers (ThorLabs PDB460C). We acquired our fringes at 100 MS/s with a two-channel data acquisition card (Signatec PX14400A), allowing detection of complex fringes from the X or Y subcircuit. Four channels would be needed for simultaneous polarization-diverse detection. We measured delays between 0 - 2.5 mm (corresponding to an RF span of 0 - 15 MHz). Since we used an AC coupled DAQ card, we achieved a highly non-linear frequency response from 0 - 3.5 MHz (corresponding approximately to delays between 0 - 0.6 mm double-pass), which allowed us to test the ability of our technique to remove large RF errors. A simple scanning microscope was constructed using a 2-axis galvo (ThorLabs GVS011) and a 40 mm objective lens (Edmund Optics) for imaging.

The second system used a novel dispersion-based swept-source operating at an 18 MHz A-line rate [10] and two balanced receivers (New Focus 1617-AC-FC). We used a two-channel 1.8 GS/s data acquisition card (Alazar ATS9360) and measured delays between 0 - 240μm (corresponding to an RF span of 0 - 350 MHz). This system allowed for confirmation of our

#230495 - $15.00 USD Received 12 Dec 2014; revised 16 Jan 2015; accepted 17 Jan 2015; published 23 Feb 2015

error compensation method for high-speed systems.

3. Mathematical framework describing errors and error-correction in passive optical quadrature demodulation circuits

In FD-OCT, an ideal optical quadrature demodulation circuit provides two quadrature signals for each polarization-diverse channel, S_I and S_Q. Note that these are electrical signals that are a function of sample number. For clarity we interchangeably represent them as a function of wavenumber, k, when solving for wavenumber-dependent errors and as a function of time, t, when solving for RF-dependent errors. In any implemented circuit, we are provided two measured fringes M_I and M_Q which are not in perfect quadrature relation. Here, we provide a generalized framework that describes how the measured fringes (M_I and M_Q) are related to the ideal fringes (S_I and S_Q) as a function of spectral and RF errors.

As a starting point, we note that quadrature refers only to a relative relationship between the I and Q signals. Thus, without loss of generality, we can initially define our ideal I signal, $S_I(k)$, as the measured fringe $M_I(k)$,

$$S_I(k) = M_I(k) \tag{1}$$

Now we seek expressions relating the ideal quadrature signal $S_Q(k)$ to the measured fringes $M_I(k)$ and $M_Q(k)$.

We first consider a polarization-based demodulation circuit wherein the birefringence of the Q path is not accurately set to achieve a 90 degrees relationship between signals. In this case, we hypothesize that the ideal Q signal can then be generally written as

$$S_Q(k) = Re[\alpha(k)M_I(k) + \beta(k)M_Q(k)] \tag{2}$$

for all conditions except that in which $M_I(k)$ and $M_Q(k)$ are equal (i.e., degenerate setting of the I and Q paths). Here, $\alpha(k)$ and $\beta(k)$ are complex wavenumber-dependent correction vectors that are related to the birefringent state of the demodulation circuit. They include both amplitude and phase errors. Importantly, the ideal signal, $S_Q(k)$, does not depend on the electrical frequency of the signal, only the wavenumber, k. Thus, the parameters $\alpha(k)$ and $\beta(k)$ are independent of the RF signal (i.e., the fringe frequency or signal depth).

Next we consider a demodulation circuit that is perfectly optimized with respect to wavenumber, i.e., $\alpha(k) = 0$ and $\beta(k) = 1$ and $S_Q(k) = M_Q(k)$. If in this circuit, the transmission length (e.g., fiber length within the demodulation circuit or electronic cable length to the digitizer) of the Q channel is longer than that of the I channel, it induces a constant propagation delay of T on the measured signal $M_Q(k)$ relative to $M_I(k)$. The effect of this delay is a phase shift in the Q channel relative to the I, but this phase shift is proportional to the fringe frequency. The framework of Eq. (2) cannot account for this error since it does not include a frequency-dependent correction. Instead, we can write the ideal Q signal as the convolution of a delta function at delay T, $\delta(\tau - T)$,

$$S_Q(t) = \int \delta(\tau - T)[M_Q(t - \tau)]d\tau \tag{3}$$

For a more general delay function (i.e. a non-constant electronic frequency responses from a low-pass filter), we can use a correction kernel $h(t)$ that describes the Q signal impulse response relative to the I signal. In this case we can write the ideal quadrature signal $S_Q(t)$ as

$$S_Q(t) = \int h(\tau)[M_Q(t - \tau)]d\tau \tag{4}$$

#230495 - $15.00 USD Received 12 Dec 2014; revised 16 Jan 2015; accepted 17 Jan 2015; published 23 Feb 2015

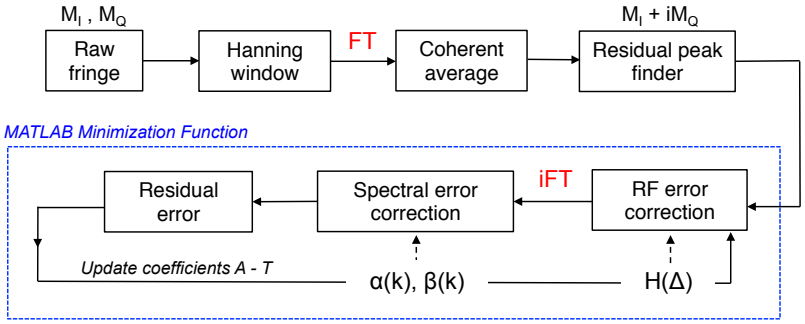

Fig. 2. Calibration algorithm flowchart outlining the steps in computing spectral ($\alpha(k)$ and $\beta(k)$) and RF ($H(\Delta)$) errors from an input of measured M_I and M_Q. A MATLAB minimization function is used to update coefficients A - T based on minimizing the residual error. If parameters M through T from $H(\Delta)$ are known, $\alpha(k)$ and $\beta(k)$ can be easily updated with inputs from a single depth.

We note that in the same way that the error described by $h(t)$ cannot be described by $\alpha(k)$ and $\beta(k)$, the error described by $\alpha(k)$ and $\beta(k)$ cannot be described by the parameter $h(t)$. Thus, both the spectral and RF errors must be corrected with Eq. (2) and Eq. (4) respectively to remove errors in quadrature demodulators.

Assuming both spectral and RF-frequency errors are present, we write a combined correction framework as

$$S_Q(k) = \frac{1}{\beta(k)} FT^{-1}\left[\frac{FT\{M_Q(t)\}}{H(\Delta)}\right] - \frac{\alpha(k)}{\beta(k)} M_I(k) \tag{5}$$

where we have moved the RF correction (Eq. (4)) to the Fourier domain via the Fourier convolution theorem. Here $H(\Delta)$ is the Fourier transform of the convolution kernel $h(t)$. We now show that correction of the measured quadrature signals via Eq. (5) sufficiently removes demodulation circuit errors.

4. Calibrating the optical demodulation circuit

In this work, we implemented an empirical approach to solving for the correction parameters ($\alpha(k)$, $\beta(k)$, and $H(\Delta)$) from measured mirror signal data. We use numerical optimization routines to solve for these parameters by maximizing extinction (maximum difference in peak power between positive and negative depth space). We first increase the SNR of our measured signals by coherently averaging a set of fringes, as we will describe in the next section. Then we perform one of two calibration procedures. The first solves for all parameters ($\alpha(k)$, $\beta(k)$, and $H(\Delta)$) and requires a series of mirror signals at depths spanning the positive and negative delay space. The second procedure assumes that $H(\Delta)$ is known and updates the correction vectors $\alpha(k)$ and $\beta(k)$ using a mirror signal at a single depth location. The general calibration process is summarized in Fig. 2.

4.1. Coherent fringe averaging

If using a single A-line, or if using multiple A-lines that are incoherently averaged, the optimization can achieve extinction ratios up to the signal SNR; extinctions greater than this will drive the power on one side of the zero delay below the noise floor. Since the extinction ratio target was 60-65 dB, it was necessary to optimize correction parameters with signals of SNR $>$65 dB. To address the challenge of obtaining such high SNR for calibration, we coherently combined multiple sequentially acquired A-lines to improve the SNR. Because the averaging is

#230495 - $15.00 USD Received 12 Dec 2014; revised 16 Jan 2015; accepted 17 Jan 2015; published 23 Feb 2015

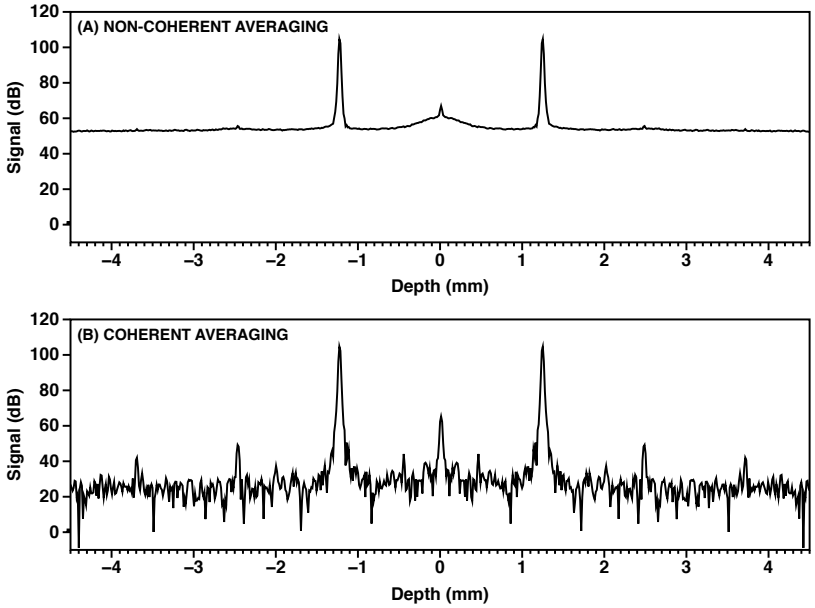

Fig. 3. (A) Incoherent averaging of 600 A-lines. (B) Coherent averaging of the same A-lines. A 28 dB improvement in SNR was achieved. The signal SNR in (B) was 75 dB, sufficient to optimize parameters to extinctions of 60-65 dB.

performed coherently, the signal amplitude is preserved but the noise floor is reduced. In swept-source OCT implementations, each A-line has phase jitter that must be compensated before averaging. We removed this phase jitter by finding the phase at the signal peak for each A-line, deriving a phase compensating array that is linear across depth and equal to the measured phase at the depth of the signal peak, and multiplying each A-line by this (complex) linear-in-depth compensating array (see Ref. [11] for a more detailed description). Either the M_I or the M_Q signal can be used to generate this phase ramp, but it is necessary to apply the same phase ramp to both the I and Q channels (in order to preserve their relative phase). The benefit of coherent averaging is illustrated in Fig. 3. In this example, the M_I signal was coherently averaged across 600 A-lines and there was an approximately 28 dB improvement (Fig. 3(B)) over a non-coherent average across the same 600 A-lines (Fig. 3(A)). Note that because only the I channel signal is plotted, peaks appear on both positive and negative depth spaces. The side-peaks outside of the point-spread function (PSF) region do not affect our optimization because the optimization procedure uses only the peak region to compute the correction parameters.

4.2. Correcting only spectral errors

To solve for the spectral correction parameters ($\alpha(k)$ and $\beta(k)$), we used a single coherently averaged mirror signal. The parameters are modeled as complex and varying quadratically with k,

$$\alpha(k) = Ak^2 + Bk + C + i[Dk^2 + Ek + F] \tag{6}$$

$$\beta(k) = Gk^2 + Hk + I + i[Jk^2 + Kk + L] \tag{7}$$

where the coefficients A through L are real-valued and k is a normalized k-vector of the fringe that spans a range from -1 to 1 (from the first point of the fringe to the last point). To test performance, we acquired 600 A-lines from each I and Q channel at -1 mm and -2.5 mm depths.

#230495 - $15.00 USD Received 12 Dec 2014; revised 16 Jan 2015; accepted 17 Jan 2015; published 23 Feb 2015

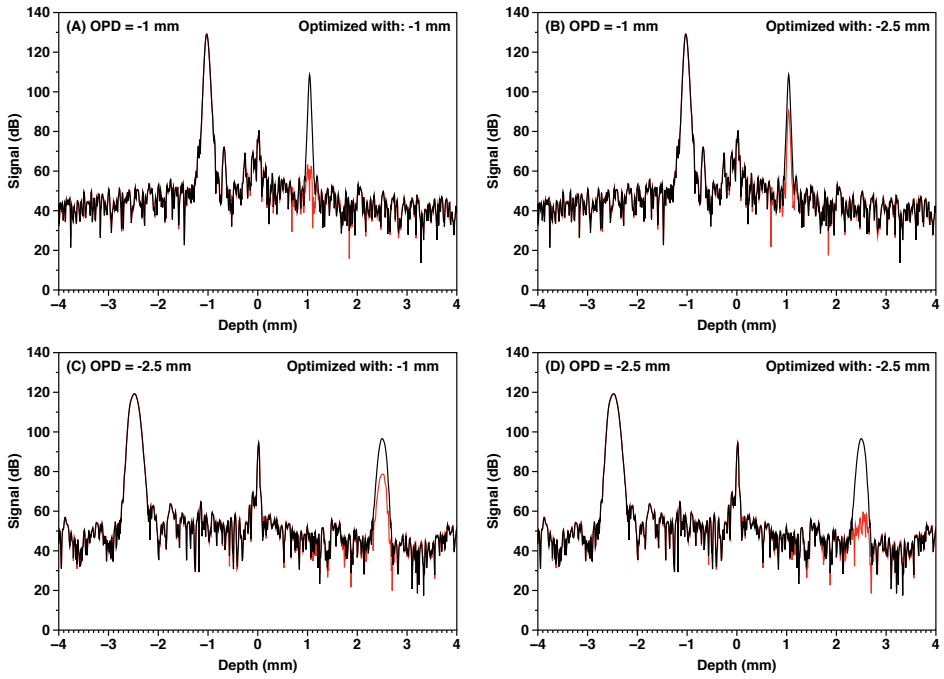

Fig. 4. Quadrature signals at two depths (-1 mm and -2.5 mm) after coherent averaging. Black = prior to spectral error calibration. Red = after spectral error calibration. (A) -1 mm PSF self-calibrated. (B) -1 mm PSF corrected with -2.5 mm error calibration. (C) -2.5 mm PSF corrected with -1 mm error calibration. (D) -2.5 mm PSF self-calibrated.

After windowing we coherently averaged to yield a pair of higher SNR M_I and M_Q fringes. The two channels were added in quadrature (M_I+iM_Q) and a simple peak finding algorithm was used to locate the the conjugate residual peak. For each depth we separately solved for coefficients A through L by setting the residual peaks as the function to be minimized through a Nelder-Mead optimization. We applied each of the two solutions to each other and show the resulting PSF prior to error removal (black) and after error removal (red) in Fig. 4. The correction parameters achieved excellent extinction (>55 dB) at the depth at which they were derived (Fig. 4(A)(D)). However, when these solutions were applied to the other depth, poor extinction was achieved (Fig. 4(B)(C)). Note that the PSF at -2.5mm is broader because this quadrature correction and optimization are done prior to fringe dechirping and dispersion correction. This demonstrates that errors can be corrected to yield accurate quadrature demodulation, but that correction based solely on the $\alpha(k)$ and $\beta(k)$ parameters within Eq. (5) is limited to a single depth location. This can be explained by the additional presence of RF errors (described by the parameter $H(\Delta)$ in Eq. (5)), as we confirm in the next section.

4.3. Correcting both spectral and RF errors

To correct for both RF and spectral errors, we include the $H(\Delta)$ parameter modeled as

$$H(\Delta) = M\Delta^3 + N\Delta^2 + O\Delta + P + i[Q\Delta^3 + R\Delta^2 + S\Delta + T] \tag{8}$$

where again Δ is a normalized depth vector ranging from -1 to +1 (from the first point of the depth spectrum to the last point). The degree of the polynomial was somewhat arbitrarily chosen, but in general should be high enough to properly model the error function (i.e. more non-

#230495 - $15.00 USD Received 12 Dec 2014; revised 16 Jan 2015; accepted 17 Jan 2015; published 23 Feb 2015

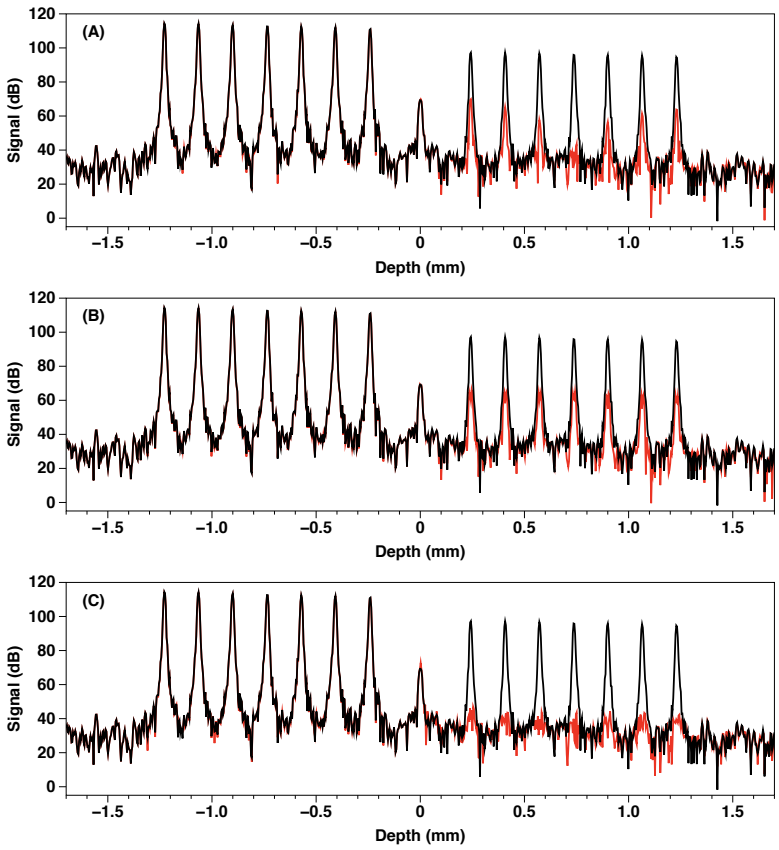

Fig. 5. PSFs without (black) and with (red) quadrature correction. Multiple depths are concatenated on the same plot for convenience, although the PSFs were recorded separately. Dechirping and dispersion correction was applied to limit PSF overlap and improve clarity. (A) Only spectral error, $\alpha(k)$, $\beta(k)$, correction. (B) Only RF error, $H(\Delta)$, correction. (C) Both spectral and RF error correction.

linearities require higher degrees). Because $H(\Delta)$ is a delay-dependent error, it was necessary to run the optimization on PSFs from multiple depths simultaneously. We acquired 600 A-lines from each of 14 mirror signals spaced in equal increments between 0.25mm - 1.25mm (data taken sequentially). Measurements from both positive and negative depth spaces were necessary to adequately constrain our algorithm. Like before, we windowed and coherently averaged the A-lines at each depth then added them in quadrature. This time, we used the summed power in the residual peaks at each depth as the function to be minimized through a Nelder-Mead optimization across coefficients A through T. This provided a single solution for $\alpha(k)$, $\beta(k)$, and $H(\Delta)$. Greater than 60 dB extinction was achieved at all depths after chirp and dispersion correction (performed as a separate calibration), as presented in Fig. 5(C). The 7 signals from the negative depth space are shown Fig. 5, however the solution was confirmed to be valid in both positive and negative depth spaces.

To confirm again that it is necessary to correct with both spectral and RF parameters, we attempted to optimize on multiple depth measurements using only spectral corrections $\alpha(k)$ and $\beta(k)$ (Fig. 5(A)), or RF correction $H(\Delta)$ (Fig. 5(B)). As expected, when only spectral corrections are applied, good extinction was achieved at one depth and as the signal moved

#230495 - $15.00 USD Received 12 Dec 2014; revised 16 Jan 2015; accepted 17 Jan 2015; published 23 Feb 2015

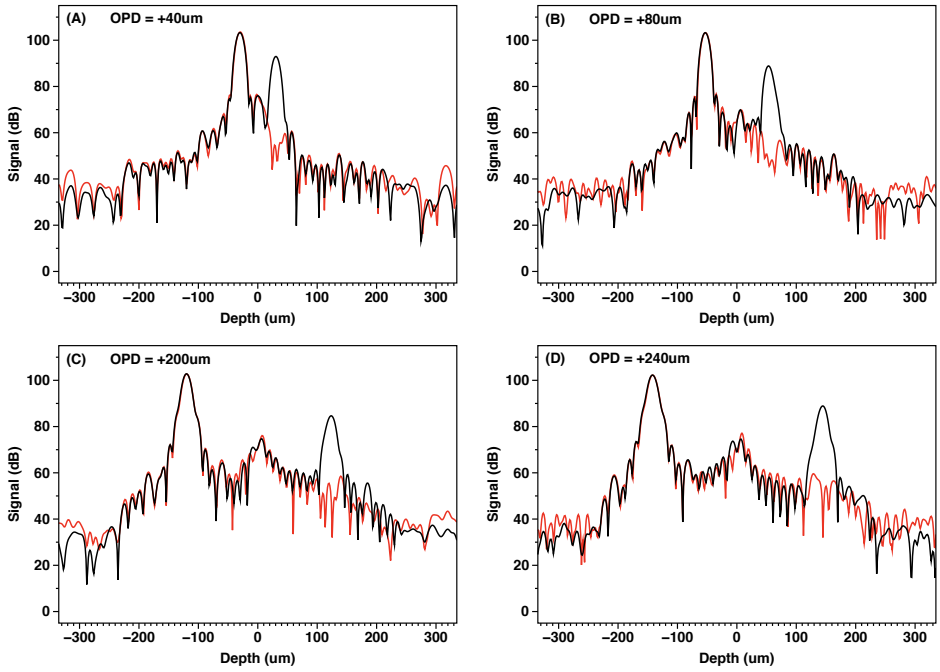

Fig. 6. The algorithm successfully removes residual errors at various depths at 18 MHz Aline rates. Black = prior to spectral error calibration. Red = after spectral error calibration. (A) +40μm (B) +80μm (C) +120μm (D) +240μm

to different depths, the RF error changed, and the correction was not longer accurate. When only RF correction was applied, poor extinction (<40 dB) was achieved at all depths because wavenumber-dependent errors were not being addressed for any depth.

To confirm that this algorithm is successful in high-speed systems, we performed a similar experiment using the high-speed laser at 18 MHz A-line rates. We measured six depths equally spaced between 40μm and 240μm with an SNR of ~45 dB after coherent averaging. The first and last two depths are displayed in Fig. 6. The signals spanned a 0 - 350 MHz RF bandwidth, a significantly larger range than our slow-speed system (0 - 15 MHz). As predicted, even small mismatches in the transmission length caused significant RF errors at these high speeds. The extinction between the primary and residual peak prior to error removal (black) visibly varies with depth as the relative phase between I and Q changes due to these mismatches. For this reason, an additional polynomial degree was added to $H(\Delta)$ to accommodate the highly varying RF error. With our algorithm we were able to removal the residual peak down to the noise floor with the same set of correction parameters (red).

5. Stability analysis

We evaluated the stability of the correction parameters obtained from the previously described calibration procedures using the polygon-based system. We acquired fringe data at 7 depth locations over 3 hours and then daily for two weeks. The system was not modified during this time. In Fig. 7, datasets from the first time point were used to calculate a complete set of correction parameters ($\alpha(k)$, $\beta(k)$, and $H(\Delta)$ and these parameters were applied to all subsequent time points. This figure shows that the achieved extinction at each depth dropped measurably within 20 minutes and continued to degrade to 50 dB over 2 hours. Over 13 days, the extinction

#230495 - $15.00 USD Received 12 Dec 2014; revised 16 Jan 2015; accepted 17 Jan 2015; published 23 Feb 2015

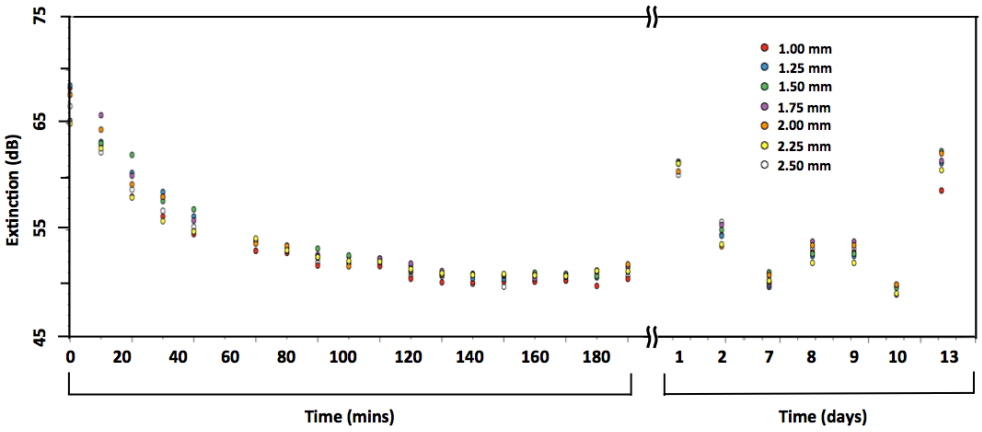

Fig. 7. Plot of the extinction for seven depths ranging from 1 mm to 2.5 mm over a period of 13 days. The depths from Time 0 mins were used to compute $\alpha(k)$, $\beta(k)$, and $H(\Delta)$ and these were used to calibrate all subsequent timepoints.

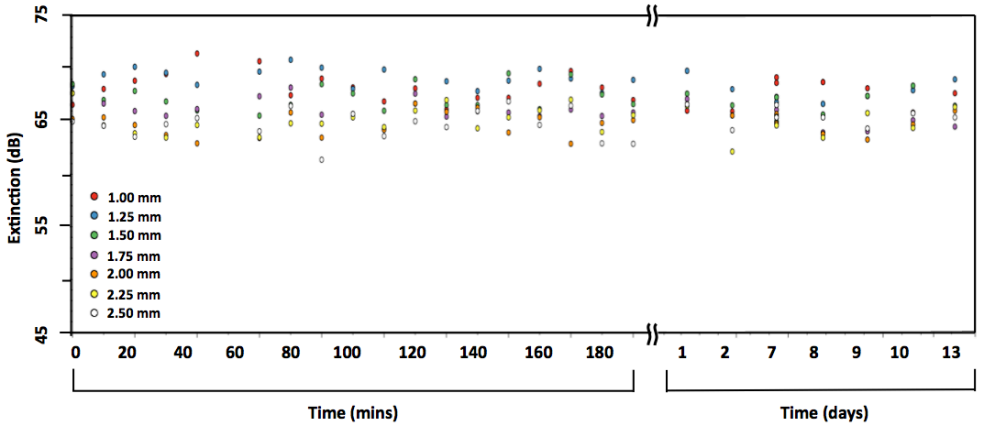

Fig. 8. Plot of the extinction for seven depths ranging from 1 mm to 2.5 mm over a period of 13 days. The depths from Time 0 mins were used to initially compute $\alpha(k)$, $\beta(k)$, and $H(\Delta)$ and $\alpha(k)$, $\beta(k)$ was renewed with depth 1.75 mm from each timepoint.

fluctuated between 50 dB and 60 dB.

To investigate the nature of the instability, we used the same longitudinal data but updated the spectral correction parameters at each timepoint (while re-using the original RF correction parameter from the first timepoint). A single coherently averaged A-line (we used 1.75 mm) was used to update the spectral correction as per Section 4.2. We note that because this required a single depth mirror signal, it was performed quickly by opening a shutter and acquiring a single frame before an imaging session. This updated spectral correction resulted in stable extinctions $>$60 dB at all time points (Fig. 8). This confirmed our prior assertion that RF errors are stable and that spectral errors need to be updated before each imaging session.

6. Imaging

Once the calibration is performed, $\alpha(k)$, $\beta(k)$ and $H(\Delta)$ values are saved and applied to images in the post-processing stage in accordance with Eq. (5). An image of a tilted IR card was

#230495 - $15.00 USD Received 12 Dec 2014; revised 16 Jan 2015; accepted 17 Jan 2015; published 23 Feb 2015

taken with the polygon-based system and a standard OCT microscope (Fig. 9). With no optical demodulation and only real-valued fringes, the conjugate ambiguity resulted in overlapping images (Fig. 9(A)). With complex fringe data obtained using the polarization demodulation circuit but without error correction, the overlap artifact is reduced by ∼25 dB but still present (Fig. 9(B)). With the demodulation circuit and our error correction algorithm, there is 65 dB removal of the artifact and the image is free of overlap (Fig. 9(C)).

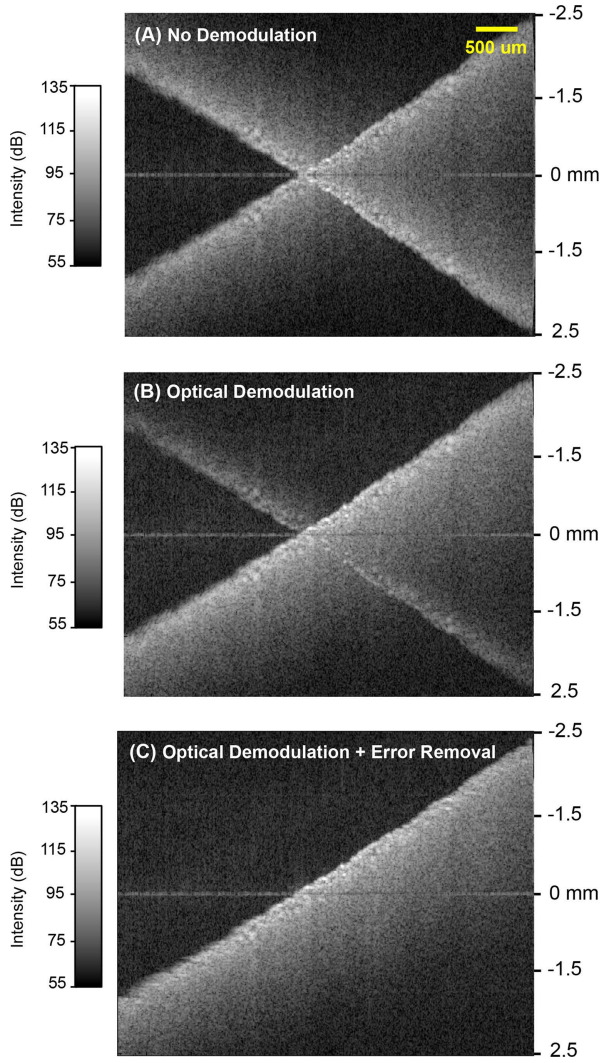

Fig. 9. Image of an IR card on a tilt so that it spans both positive and negative depth spaces; the vertical axis is depth. (A) No optical demodulation used. (B) Optical demodulation with a polarization-demodulation circuit alone. (C) Optical demodulation with a polarization-demodulation circuit and our error removal algorithm.

7. Conclusion

Two broad comments are relevant for the practical use of quadrature demodulation methods and error correction in OCT imaging. First, as we described in Section 4.3, it is critical that

#230495 - $15.00 USD Received 12 Dec 2014; revised 16 Jan 2015; accepted 17 Jan 2015; published 23 Feb 2015

when computing both spectral and RF error parameters, fringe signals from both sides of the zero delay are used. We observed that optimization on multipe depth signals that are all located on one side of the zero delay location could not achieve high extinction for signals located on the other side of the zero delay. However, for only spectral correction parameters, a single depth location signal on either the positive or negative space is sufficient. Second, the form of Eq. (5) implies an apparent computational cost to performing spectral and frequency correction (i.e., applying the correction once the parameters are known). However, we note that in systems that utilize computational chirp correction, these FFT steps are already performed as part of the interpolation procedure [12]; our quadrature error correction can be embedded within this procedure. In this scenario, the additional computational burden associated with applying this correction is small relative to that burden associated with dechirping and dispersion correction. For systems utilizing hardware resampling (k-clocking) the additional computational burden of corrected quadrature demodulation is more significant.

In this work, we have demonstrated that it is possible to computationally eliminate complex conjugate ambiguity from imperfect quadrature signals. The presented method solves for correction parameters based on either one mirror signal (for spectral parameters alone), or a set of mirror positions (for both RF and spectral parameters together). Although the latter dataset takes more time to acquire (up to 30 minutes using a manual method), it is performed infrequently as long as the hardware is unchanged. The former dataset needs to be acquired prior to each imaging session and takes less than a few seconds if a sample mirror is already built in. Once the empirical datasets have been collected, the time for computation of error correction terms based on these datasets is a few minutes. The correction parameters can be applied to images in the post-processing stage and can be integrated into real-time displays. We investigated the stability of the correction parameters and showed that spectral errors are stable over the duration of an imaging experiment (minutes), and RF errors are stable across time periods exceeding 13 days. We predict that the SNR change due to the error correction technique is small, however we have not compared this to other passive demodulation techniques and aim to investigate this in future works. The correction algorithm developed in this work enables high-extinction complex demodulation that is compatible with balanced detection, polarization-diverse detection, high-speed imaging, and broadband imaging.

Acknowledgments

Research reported in this publication was supported in part by the Center for Biomedical OCT Research and Translation through Grant Number P41EB015903, awarded by the National Institute of Biomedical Imaging and Bioengineering of the National Institutes of Health. And by the NSF-GRFP, Martinos Scholarship, Wellman Center for Photomedicine Graduate Fellowship, and the National Institutes of Health under award number R01CA163528.

#230495 - $15.00 USD Received 12 Dec 2014; revised 16 Jan 2015; accepted 17 Jan 2015; published 23 Feb 2015